2024 SPE Improved Oil Recovery Conference

SPE-218179-MS

Aqueous Nanobubble Dispersion of CO_2 for Enhanced Oil Recovery – Coreflooding and Huff-n-Puff Experiments

Tesleem Lawal, Hao Wang, Abouzar Mirzaei-Paiaman, and Ryosuke Okuno

The University of Texas at Austin, Austin, Texas, USA

Abstract

This paper presents an experimental study of aqueous nanobubble dispersion of carbon dioxide (CO_2-NB) for enhanced oil recovery. CO_2-NB was compared with brine and slightly supersaturated carbonated water (eCW) in corefloods with Berea sandstone cores and dead oil at room temperature. CO_2-NB was also compared with a mixture of CO_2 and brine with no NB in high-pressure high-temperature huff-n-puff experiments with live oil-saturated tight Kentucky sandstone cores using three different fracture-matrix configurations.

Coreflooding results showed that the displacement of oil by CO_2-NB yielded a delayed breakthrough, in which the oil recovery factor at breakthrough (RF_{BT}) was 9.1% original-oil-in-place (OOIP) greater than RF_{BT} in the brine case. The displacement of oil by eCW did not show such an increase in RF_{BT}, but showed a long-term gradual increase in oil recovery after the breakthrough. The increased RF_{BT} by CO_2-NB can be attributed to the nucleation of a CO_2-rich phase near the displacement fronts, where the metastable aqueous phase releases CO_2 to the oleic phase while the nanobubbles of CO_2 with capillary pressure release CO_2 to the surrounding aqueous phase. That is, the partially miscible displacement of dead oil by the in-situ generated CO_2-rich phase could have enhanced RF_{BT} by CO_2-NB in comparison to the immiscible oil displacement by water in the brine case. Huff-n-puff experimental results showed a systematic increase in oil recovery by using CO_2-NB in comparison to CO_2-brine (with no NB). In the CO_2-NB case, the annular, artificial, and combination fractures had oil recoveries of 34%, 36%, and 39% OOIP, respectively. In the CO_2-brine case, they were 24.5, 22%, and 28% OOIP, respectively.

1. Introduction

Carbonated water injection (CWI) has been studied as CO_2-augmented waterflooding, in which the injection brine is partially or fully saturated with CO_2 (Seyyedi et al. 2017). Studies have shown that CWI can increase oil recovery in comparison to waterflooding with no CO_2. The main mechanisms of oil recovery by CWI reported in the literature include oil swelling, oil viscosity reduction, nucleation of a new gaseous phase, and wettability alteration (Riazi et al. 2009; Kechut et al. 2010; Sohrabi et al. 2015; Ruidiaz et al. 2018; Ghandi et al. 2019; Ghosh et al. 2022; Vadhan and Phukan 2022). Oil recovery mechanisms of CWI are also expected to occur during conventional CO_2 flooding and CO_2-based water-alternating-gas flooding where CO_2 dissolution in the in-situ brine spontaneously occurs (Sohrabi et al. 2015).

The effects of CW on oil recovery by spontaneous imbibition have been studied using carbonate and sandstone cores. Grape et al. (1990) showed that the CO_2 dissolved in the imbibed water improved both the imbibition rate and the recovery efficiency. They reported that a 1-wt% CW solution recovered an additional 8% original-oil-in-place (OOIP) and 16% OOIP in a 76 mD sandstone and a 7 mD limestone, respectively, for a soak time of 72 hours. Similarly, Perez et al. (1992) found enhanced oil recovery rates and ultimate oil recoveries with the imbibition of CW than with the control experiment using brine with no CO_2. Seyyedi and Sohrabi (2016) conducted spontaneous CWI experiments on carbonate and sandstone cores and concluded that the main mechanisms of enhanced oil recovery (EOR) were oil swelling, oil viscosity reduction, oil-brine IFT reduction, mineral dissolution, and wettability alteration toward a more water-wet state. They also found wettability alteration by CW to be stronger in carbonate rock than in sandstone rock. Overall, CWI caused favorable CO_2-rock-brine interactions such as rock wettability alteration from oil-wet to water-wet, which, in turn, enhanced water imbibition for a more efficient displacement of oil by CW (Seyyedi et al. 2015; Zhang et al. 2018; Chen et al. 2019; Drexler et al. 2020). The altered wettability has been attributed to the proton-promoted dissolution of surface minerals in the tested cores.

For their CWI experiments at 13.8 MPa (2000 psia) and 38°C, Sohrabi et al. (2011) reported the CO_2 content in the brine to be 28.7 scc CO_2 per cc brine (1.24 mol/L) and estimated the solubility of brine to be approximately 30 scc CO_2 per cc brine (1.29 mol/L). Sohrabi

et al. (2015) conducted a series of CWI core flooding experiments using dead and live crude oil. They stated that wettability alteration caused by the dissolution of CO_2 in oil and the destabilization of polar oil components was a contributing EOR mechanism. Seyyedi et al. (2015) investigated rock wettability alteration by CW through a series of high-pressure high-temperature contact angle experiments. Their results showed that CW had a significant impact on rock wettability and the extent of wettability alteration was correlated to the CO_2 concentration in brine as well as the initial wettability state of the rock.

Sohrabi et al. (e.g., Seyyedi and Sohrabi 2017; Seyyedi et al. 2017ab; Seyyedi et al. 2018) presented pioneering studies on CWI using high-pressure micromodel experiments. They discovered that the mass transfer of CO_2 upon the contact of CW with the in-situ oil caused the nucleation of a gaseous phase, which occurred more rapidly in live oil experiments than in dead oil experiments. The new phase contributed to EOR because of oil swelling and reduced residual oil (trapped oil) in their micromodel experiments. Slim-tube experiments using CW and brine as the control experiment showed that the CO_2 breakthrough occurred after the water breakthrough (Seyyedi et al. 2017). This is consistent with their oil recovery histories for the two cases, where the incremental oil recovery by CWI occurred gradually after the water breakthrough. The slim-tube oil recovery by CWI was 24%OOIP greater than the brine case at 5.0 pore-volumes injected (PVI). Such a long-term impact of CO_2 on oil recovery in CWI was also shown by LaForce and Orr (2009), who presented analytical solutions of water-CO_2 co-injection in a quaternary system using the method of characteristics (MOC). They showed that the miscibility development in water-CO_2 co-injection requires the CO_2 concentration in the injection fluid to exceed the minimum gas fraction (MGF) so that multiple contacts can develop the miscibility between the injected CO_2 and the oil at the displacement front under one-dimensional convection-dominant flow in a quaternary system.

Among many experiments by Sohrabi et al., one experiment presented by Sohrabi et al. (2015) implied a possibility that the CO_2-rich phase generated near the fronts of oil displacement yielded a markedly increased oil recovery factor upon breakthrough (RF_{BT}) in comparison to the control experiment with brine with no CO_2. Seyyedi et al. (2017) observed that the mass transfer of CO_2 from CW to the in-situ oil near the displacement front was quite rapid. In the particular experiment by Sohrabi et al. (2015), therefore, the mobility of the CO_2-rich phase could have exceeded that of the water phase locally near the displacement front, although the CO_2 concentration in CWI was likely below the MGF as defined in LaForce and Orr (2009). Such local phenomena near the displacement front depend on the phase nucleation kinetics and extent, flow velocity, relative permeability, and fluid properties among many other factors.

The central hypothesis in this research is that the CO_2-rich phase generated near the fronts of oil displacement in CWI can greatly contribute to oil recovery by supersaturating the injection brine with CO_2. The research is primarily focused on enhancing the mechanism associated with the nucleation of a CO_2-rich phase, in which a greater amount of oil is displaced by the CO_2-rich phase than by the water phase in CWI. Increasing the CO_2 concentration in water is also expected to enhance other mechanisms, such as rock wettability alteration.

One potential method of increasing the CO_2 concentration in water is to generate aqueous nanobubble (NB) dispersion. NBs have diameters below 1.0 μm, and their sizes vary with pressure, temperature, brine composition, and other operating conditions used to generate them (Temesgen et al. 2017). Aqueous NB dispersion is known to possess unique properties, such as high stability, solubility, and the ability to modify interfaces, and has been applied in various industrial processes (Ebina et al. 2013; Perez Sirkin et al. 2019; Favvas et al. 2021). However, applications of aqueous NB dispersion are limited to low-pressure open systems, such as agricultural applications (Pal et al. 2022), wastewater treatments (Atkinson et al. 2019; Lyu, et al. 2019), surface cleaning, and material separation (Zhu et al. 2016). Aqueous NB dispersion for low-pressure applications can be generated by various methods, such as water electrolysis, cavitation, porous (glass, ceramic, stainless steel) membrane filters, and by mixing gas and water (Hernandez Aguilar et al. 2006; Kukizaki and Goto 2006; Kikuchi et al. 2006, 2007, 2009; Ohgaki et al. 2010; Smirnov and Berry 2015; Ahmed et al. 2018; Oliveira et al. 2018; Ulatowski et al. 2019). Their size and concentrations are observed using image analysis techniques such as nanoparticle tracking analysis (NTA), dynamic light scattering (DLS), and scanning electron microscopy (SEM). Zeta potential measurements showed that the surfaces of NBs are negatively charged.

Previous studies and applications of aqueous NB dispersion are limited to low-pressure open systems. Recently, Wang et al. (2023) and Achour et al. (2024) presented experimental data of aqueous NB dispersion with CO_2 and nitrogen at high pressures relevant to subsurface applications [up to 21 MPa in Wang et al. (2023) and up to 28 MPa in Achour et al. (2024)]. Their experimental data showed that the gas concentration in aqueous NB fluid increased substantially with pressure. That is, aqueous NB fluid may find more promising applications at high pressures. Achour et al. (2024) presented a thermodynamic model for aqueous NB fluid using minimization of the Helmholtz free energy with the GERG-2008 equation of state. They modeled aqueous NB fluid as two phases with a cluster of NBs and the external aqueous phase that is supersaturated by the gaseous species. That is, the gaseous species are present in the system in two modes: a cluster of NBs and molecule dispersion in the aqueous phase. Their thermodynamic analysis of aqueous NB dispersion showed that the cluster of NBs was not the main contribution to the enhanced gas content, but the presence of NBs with capillary pressure enabled the elevated level of gas supersaturation of the aqueous phase.

Wang et al. (2024) presented a novel application of aqueous NB dispersion of CO_2 for CO_2 mineralization with basalt. However, the literature is scarce on aqueous NB dispersion for EOR. This paper presents for the first time high-pressure coreflooding and huff-n-puff (HnP) experiments using aqueous NB dispersion of supercritical CO_2 (CO_2-NB). The corefloods used Berea sandstone cores with dead oil, and the HnP experiments used tight sandstone cores with live oil. The CO_2-NB was generated using the method presented by Wang et al. (2023); hence, the fundamental properties of CO_2-NB could be derived, including bubble size, number density, and CO_2 content. In what follows, we first present the materials and methods, and then present the main results and discussions of the oil recovery performance of CO_2 NB dispersion. Finally, we give the main conclusions of this research.

2. Materials and Methods

2.1. Fluid Properties

The experiments in this research consisted mainly of coreflooding at room temperature and huff-n-puff (HnP) at reservoir temperature (102°C). The former used a dead oil sample, for which properties are given in Table 1. The latter used a recombined live oil sample prepared by mixing the dead oil sample with a solution gas mixture (Table 2) for a tight sandstone reservoir. The mixing ratio of the dead oil and solution gas was 56.95 mol% and 43.05 mol%, respectively. The live oil bubble point pressure was 14.4 MPa (2090 psia). Detailed properties of the live oil can be found in Appendix A. The pressure and temperature for the target reservoir were 24.2 MPa (3515 psia) and 102°C, respectively.

Data from PVT experiments, including constant mass expansion and swelling tests, were used to calibrate the Peng-Robinson equation of state (EOS) for CO_2/dead-oil and CO_2/live-oil mixtures using the method of Kumar and Okuno (2016). The calibrated EOS model showed a transition from V-L_1 to V-L_1-L_2 to L_1-L_2 with increasing pressure within the multiphase region in the pseudo-Px diagram for dead oil and CO_2 at room temperature, where V is the vapor phase, L_1 is the oleic phase, and L_2 is CO_2-rich liquid phase (see Appendix A). This type of phase behavior was expected for this mixture at room temperature as it is known for low-temperature CO_2 flooding (Okuno et al 2011; Okuno and Xu 2014). The L_1-L_2 immiscibility was calculated even at 69 MPa (10,000 psia). As for the live oil used for HnP experiments, the thermodynamic minimum miscibility pressure (MMP) with pure CO_2 at reservoir temperature (102°C) was calculated to be 17.5 MPa (2540 psia) using a mixing cell method (Ahmadi and Johns 2011; Li et al. 2015).

Table 1—Composition of the dead oil sample used in this research

Component	C_1	C_2	C_3	C_4	C_5	C_6	C_{7+}
Mole %	0.000	0.000	0.208	1.357	3.813	6.362	88.26
Molecular weight (g/mol)	183						
Density (g/mL)	0.804 [at 13.8MPa (2000 psia) and 22°C]						
Viscosity (cP)	2.7 (at 22°C)						

Table 2—Composition of the solution gas mixture used in this research

Component	C_1	C_2	C_3	C_4	C_5	C_6	C_8
Mole %	92.90	4.331	1.230	0.8213	0.4107	0.1699	0.1365

As for bines, the corefloods used 5-wt% (50,000 ppm) NaCl and the HnP experiments used "reservoir brine (RB)" as given in Table 3. The carbonated NaCl brine was prepared by mixing CO_2 with the NaCl brine in an accumulator equipped with a stirrer (mixing accumulator) at 13.9 MPa (2015 psia) and 22°C. The mixing accumulator was connected to a Teledyne ISCO syringe pump during mixing, and the CO_2 saturation was set when the pump flow rate stabilized. The density of the CW was measured to be 1.053 g/mL at 13.8 MPa (2004 psia). The molar composition of the carbonated water sample was determined to be 2.98 mol% CO_2 and 97.02 mol% NaCl brine, which corresponds to a CO_2 concentration of 1.46 mol/L, based on the experimental procedure of Wang et al. (2023). The inherent solubility of CO_2 in 5-wt% NaCl brine was calculated to be 1.19 mol/L at 13.8 MPa and 22°C using PHREEQC (Parkhurst and Appelo 2013). This value is in agreement with the model developed by Duan and Sun (2003). That is, the carbonate brine was supersaturated by CO_2 beyond the inherent solubility. In fact, many experiments using carbonated water/brine at different conditions in our research have indicated that the mixing of gases and water tends to cause micro- and nano-scale bubbles observed by light scattering. Such bubbles are kinetically stable for weeks and months even in an open system (Oh and Kim 2017; Jadhav and Barigou 2020). Hence, it is quite conceivable that the mixing at 13.9 MPa caused a certain level of supersaturation by CO_2. Therefore, the carbonated water sample used in the corefloods is referred to as "enhanced carbonated water" or eCW to differentiate it from other carbonated water floods studied in the literature.

Table 3—Composition of the RB used in this research (TDS = 66,703 ppm)

Ions	Na^+	Ca^{2+}	K^+	Mg^{2+}	Sr^{2+}	Ba^{2+}	Mn^{2+}	Cl^-	SO_4^{2-}
ppm	17,883	6560	427	401	357	14	9.3	41,045	7

The aqueous CO_2 nanobubble (CO_2-NB) was prepared for coreflooding (22°C) and HnP experiments (102°C). Since the solubility of CO_2 in water increases with decreasing temperature, the CO_2-NB sample for the corefloods was prepared by pre-saturating NaCl brine with CO_2 at 27.7 MPa (4015 psia) and then co-injecting the CO_2-saturated brine and CO_2 at an equal volumetric rate of 100 mL/hr (in total, 200 mL/hr) at 13.9 MPa (2015 psia) into a core holder that contained three stainless-steel porous membranes. Each membrane had a porosity of 37%, an average pore size of 5 μm (with a maximum size of 10 μm), an outer diameter of 25.4 mm and a length of 3 mm. The confining pressure was 17.3 MPa (2515 psia) for the core holder, which was maintained using a hydraulic manual pump. After the co-injected fluids passed through the core holder, they were received into an accumulator downstream of the core holder. This accumulator contained both excess bulk CO_2 and CO_2-NB. The excess bulk CO_2 was removed by transferring it to another accumulator through an inline density-meter that was used to quantitatively detect the boundary between CO_2 and CO_2-NB. The density of the CO_2-NB sample in the accumulator was 1.053 g/mL at 14.2 MPa (2055 psia) and was then used for injection. The overall composition of the CO_2-NB sample was estimated to be 3.87 mol% CO_2 and 96.13 mol% NaCl brine based on Wang et al. (2023). This overall composition corresponded to a CO_2 concentration of 1.87 mol/L, which is 57% greater than the inherent solubility of CO_2 and 28% greater than the eCW sample.

For the CO_2-NB sample used for the HnP experiments, RB and CO_2 were co-injected into three porous membranes at a volumetric flow rate of 90% CO_2 and 10% RB (in total, 25 mL/hr) at 24.2 MPa (3515 psia) at 102°C without the pre-saturation step. The overall molar composition of the sample used in the HnP experiment was not measured because the injection process of the CO_2-NB sample into the test cell was designed specifically for a certain field project.

2.2. Core Properties

The coreflooding experiments used Berea sandstone (BSS) cores of approximately 25.4 mm in diameter and 229 mm in length. The HnP experiments used Kentucky sandstone (KSS) cores of approximately 38.1 mm in diameter and 152 mm in length. X-ray diffraction (XRD) analysis showed that the Kentucky sandstone cores consisted of 76.5% quartz and 23.5% albite.

The porosities and permeabilities of the BSS cores were determined at 22°C. Each core was first evacuated for one hour and its effective porosity was determined by saturating it with NaCl brine. Then, NaCl brine was injected through each core at 100, 80, and 60 mL/hr to determine the permeability from the measured differential pressure. Initial oil and water saturations (S_{oi} and S_{wi}) were determined by displacing NaCl brine with dead oil at a constant flow rate of 10 mL/hr until negligible brine production. The flow rate gave a Rapoport-Leas number 0f 4.03 cP-cm^2/min, which was greater than the 3.0 cP-cm^2/min for controlling the capillary end effect.

The porosities of the KSS cores were determined by first injecting helium into each core at 7.0 MPa (1015 psia) to determine the pore volume and then dividing the pore volume by the bulk volume of the core. The permeabilities were determined by injecting helium and measuring differential pressures at a steady state. Each core was first evacuated for 12 hours, and the system was heated up to 102°C. After the temperature stabilized, the system was filled with live oil at 31.1 MPa (4515 psia) with no water saturation (S_{wi} = 0). To determine the original oil in place (OOIP), a test saturation was performed on a separate core with similar properties as the six cores used. This test core was first saturated with live oil as described above and then removed from the system. The mass of the core was measured before and after the saturation. The volume of oil in the core was computed at atmospheric pressure and room temperature using the measured mass and the density of dead oil. Based on the volume calculations, it was determined that 73.4% of the core was saturated with dead oil. This preliminary experiment served as the baseline for determining OOIP during the saturation of the KSS cores used in the experiments. For all the other KSS cores used in the experiments, the OOIP was determined as 73.4% of the respective pore volumes. Table 4 summarizes the properties of the cores used in this research.

Table 4—Properties of the cores used in this research

Property	BSS #1	BSS #2	BSS #3	KSS #1	KSS #2	KSS #3	KSS #4	KSS #5	KSS #6
Length (cm)	22.8	22.9	22.9	14.8	15.1	15.3	15.2	14.8	14.8
Diameter (cm)	0.97	0.97	0.97	3.81	3.81	3.81	3.81	3.81	3.81
Porosity, ϕ	0.206	0.208	0.209	0.157	0.140	0.119	0.124	0.149	0.145
Permeability, k (mD)	102	107	107	0.66	0.66	0.53	0.53	0.54	0.63
Pore volume, V_p (mL)	22.3	22.6	22.7	26.4	24.1	22.5	23.2	24.1	23.2
Initial water saturation, S_{wi}	0.652	0.615	0.614	—	—	—	—	—	—
Initial oil saturation, S_{oi}	0.348	0.385	0.386	0.734	0.734	0.734	0.734	0.734	0.734
Original oil in place, OOIP (mL)	14.6	13.88	13.97	19.36	17.66	16.52	17.00	17.70	17.06

2.3. Coreflooding Experiments

Three sets of coreflooding experiments were performed to compare the displacements of dead oil by brine, eCW, and CO_2-NB in BSS cores at 22°C. Figure 1 shows a schematic of the experimental setup. The system consisted of a vertically mounted Hassler-type core holder, three Teledyne ISCO pumps, five accumulators for dead oil, NaCl brine, eCW, CO_2-NB, and nitrogen, a hydraulic manual pump to apply a confining pressure, a back pressure regulator (BPR), pressure gauges, graduated cylinders, and an oven. The confining pressure was set at 18.7 MPa (2715 psia) and the back pressure was set at 15.3 MPa (2215 psia). The eCW and CO_2-NB samples were prepared at 13.9 MPa (2015 psia), and the back pressure kept the system pressure greater than 13.9 MPa (2015 psia) to avoid liberating CO_2 from eCW and CO_2-NB. The effluent samples were collected at 22°C and atmospheric pressure.

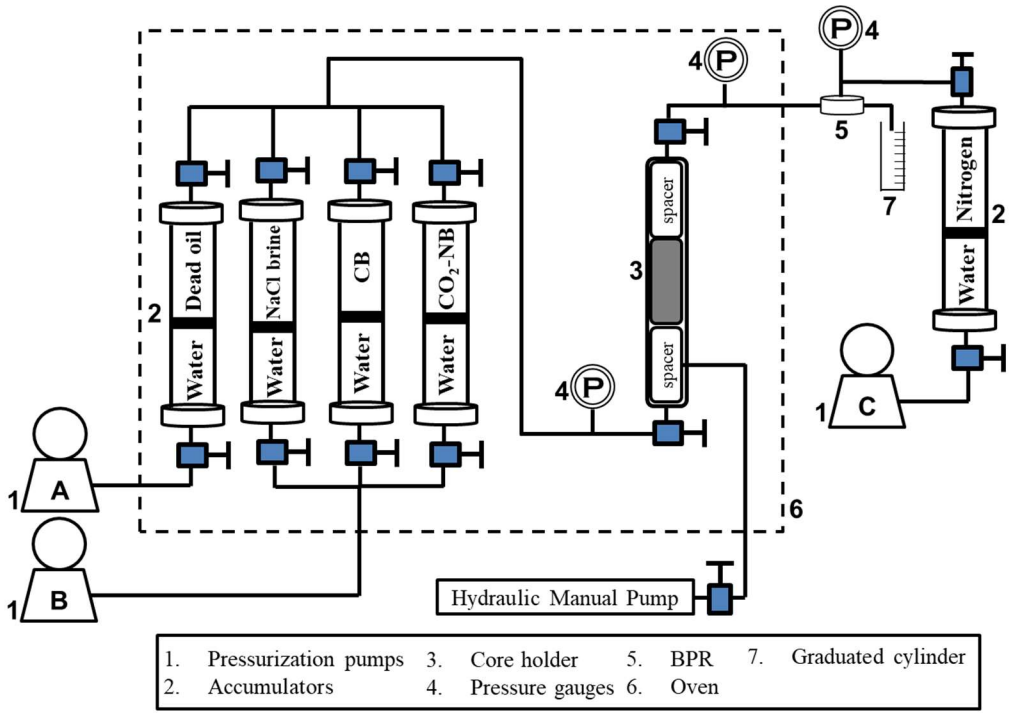

Figure 1—Schematic of coreflooding setup for the secondary NaCl brine, carbonated brine, and CO_2-nanobubble coreflooding experiments with dead oil.

After establishing S_{oi} and S_{wi}, NaCl brine, eCW, or CO_2-NB was injected through the core at a constant flow rate of 4 mL/hr until no further oil production occurred for one pore volume (PV). The differential pressure across the core was recorded at intervals during the injection.

2.4. Huff-n-Puff Experiments

Six HnP experiments were performed using the KSS cores saturated by live oil at 102°C. The primary factors studied were CO_2-NB and fracture/matrix configuration, both of which affected the amount of CO_2 injected during the huff-n-puff experiments as will be shown later. Three sets of experiments with CO_2-NB and without NB (CO_2-RB) had the following fracture/matrix configurations: an annular fracture (set 1), an artificial fracture along the longitudinal axis (set 2), and a combination of an annular and an artificial fracture (set 3). Figure 2 schematically summarizes the fracture-matrix configurations for the six HnP experiments.

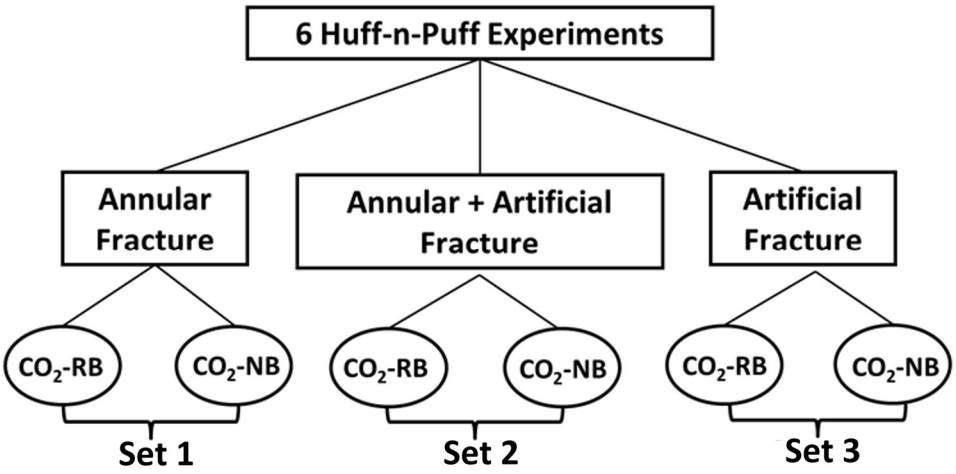

Figure 2—Summary of the huff-n-puff experiments conducted in this research.

Experiment sets 1 – 3 had different areas of exposure to the injected fluids during HnP. For each set, the setups for CO_2-NB and CO_2-RB had similar surface areas. Set 3 had the largest exposed surface area (268 cm^2), followed by Set 1 (201 cm^2), and then Set 2 (108 cm^2). The cores in Sets 1 and 3 were placed in an in-house HnP cell while the cores in Set 2 were placed in a Hassler-type core holder.

One way to characterize the fracture/matrix configurations is to use a characteristic length representing the ratio of matrix volume to surface area; for example,

$$\lambda = \frac{V_b}{A_s} \tag{1}$$

where λ is the characteristic length, V_b is the matrix volume, and A_S is the surface area. The λ value was 0.845 for Set 1, 1.52 for Set 2, and 0.602 for Set 3.

Figures 3 and 4 show the schematics of the HnP experiments. For the CO_2-RB experiments, the setup consisted of a test cell (a HnP cell for sets #1 and #3; a core holder for set 2) that contained a KSS core, accumulators for nitrogen, RB, sCO_2, and live oil, three (3) Teledyne ISCO pressurization pumps, several pressure gauges, a back-pressure regulator (BPR), graduated cylinders, and an oven. An additional accumulator (the receiver) was placed inside the oven and connected to the top of the test cell to collect the produced fluids. The produced fluids were allowed to stabilize in the receiver accumulator for two hours before being recovered. Because the fluids were recovered at reservoir pressure, a BPR was placed at the outlet of the tubing system to maintain the upstream pressure at reservoir temperature while the produced fluids were recovered at atmospheric pressure and room temperature. The upstream pressure was regulated using nitrogen. One pump was used to maintain the pressure in the CO_2 accumulator, and another was used to maintain the pressure in the receiver accumulator while the third pump was used to maintain pressure in the live oil and RB accumulators.

The setup for the CO_2-NB experiments was similar to that for the CO_2-RB experiments except that an additional core holder (with its hydraulic manual pump for confining pressure control) was placed between the RB and CO_2 accumulators and the test cell. This core holder housed the membranes to generate aqueous NB dispersion of CO_2. Three pieces of the membrane were placed between the two spacers inside the core holder. The overburden pressure of the core holder was maintained with a hydraulic manual pump. The setup for set 3 was the same as that of set 1; the only difference was the fracture/matrix configuration.

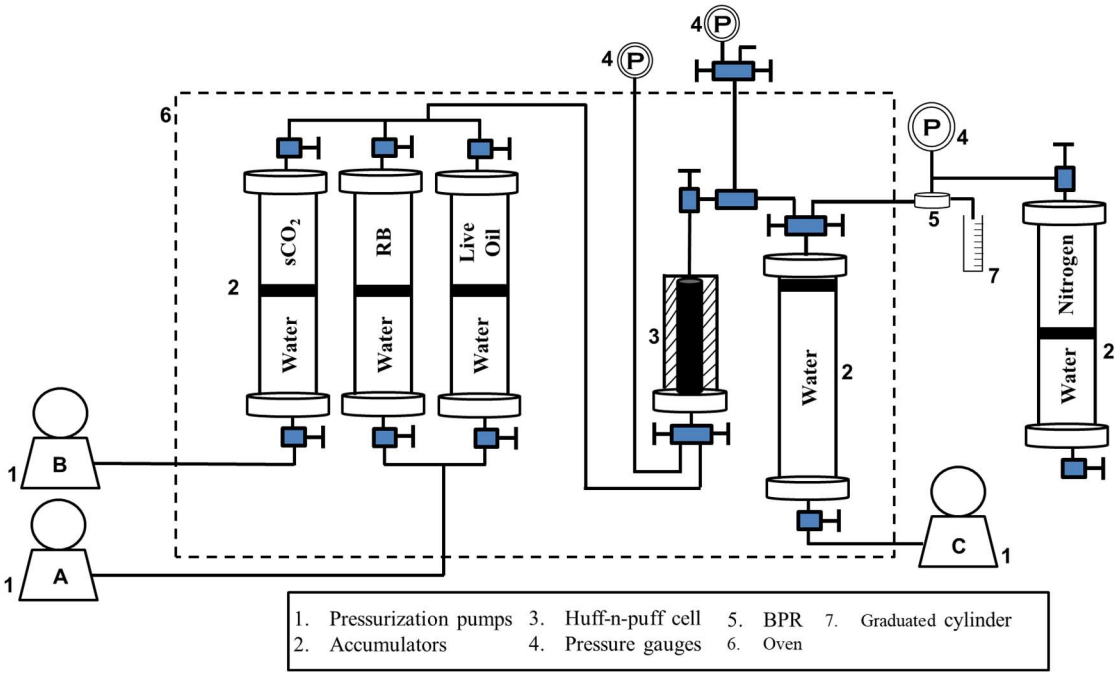

Figure 3—Schematic of the huff-n-puff experimental setup for CO_2-RB (without NB) sets 1 and 3. In set 2, the HnP cell was replaced with a horizontally mounted core holder.

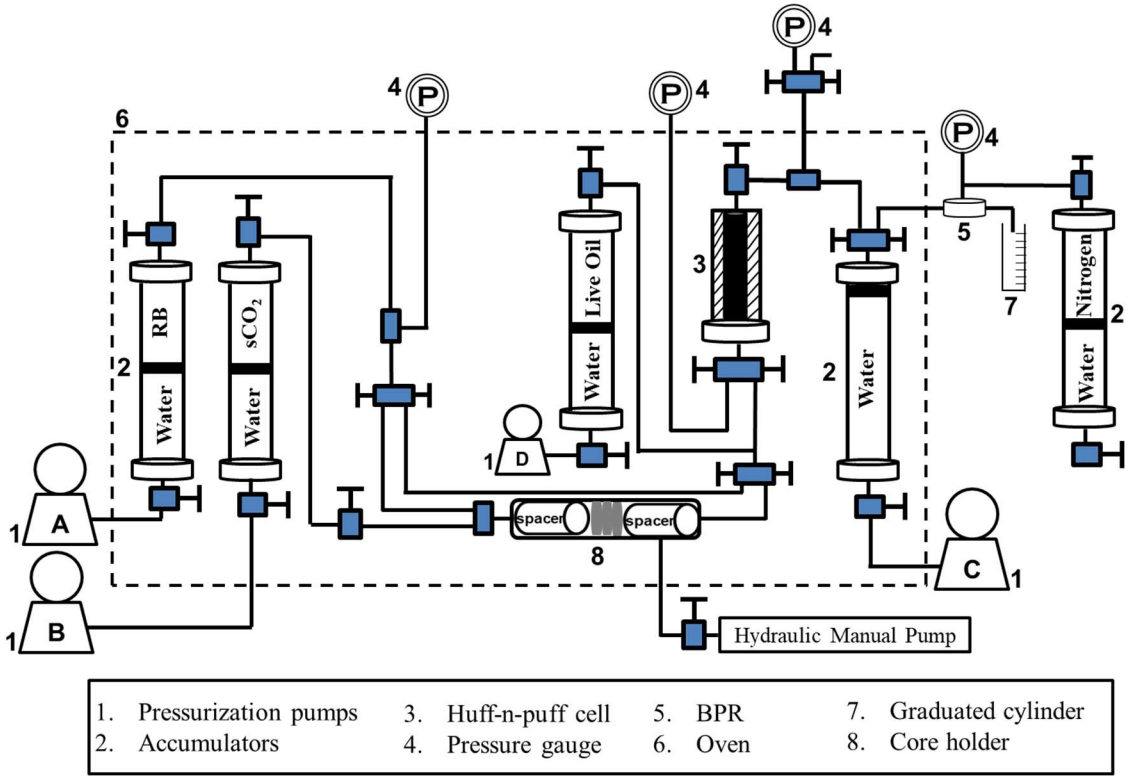

Figure 4—Schematic of the huff-n-puff experimental setup for CO_2-NB (with NB) sets 1 and 3. In set 2, the HnP cell was replaced with a horizontally mounted core holder.

Two HnP experiments were performed for each set (1 – 3): CO_2-RB and CO_2-NB. The experiments were performed at 24.2 MPa (3515 psia), which was above the thermodynamic MMP (17.5 MPa), at 102°C. Each experiment consisted of a RB injection stage and several HnP cycles. For the CO_2-RB sets, CO_2 and RB were injected simultaneously into the test cell during the injection stage. During the RB stage, RB was injected at 25 mL/hr and 24.2 MPa (3515 psia) for 2.0 fracture volumes (FV) so that the HnP cell could be filled with RB. Then, the RB was shut in at 31.1 MPa (4515 psia) for 13 hrs. After the shut-in period, RB was injected at 25 mL/hr and 24.2 MPa (3515 psia) for 2.0 FV to displace the fluids in the fracture volume. For the HnP cycles after the RB stage, CO_2 and RB were

simultaneously injected at 25 mL/hr with a volumetric ratio of 90% CO_2 and 10% RB (corresponding to 22.5 mL/hr for CO_2 and 2.5 mL/hr for RB) for 2.0 FV. Then, the system was shut-in at 31.1 MPa (4515 psia) for 13 hrs. After this shut-in period, RB was injected at 25 mL/hr and 24.2 MPa (3515 psia) to displace the fluids in the HnP cell. The volumetric ratio used for CO_2 and RB was determined for a certain field project as mentioned previously.

For the CO_2-NB sets, CO_2 and RB passed through the membranes and the resulting CO_2-NB entered the test cell. During the initial RB stage, RB was injected at 25 mL/hr and 24.2 MPa (3515 psia) for 2.0 fracture volumes (FV). Then, the RB was shut in at 31.1 MPa (4515 psia) for 13 hrs. After the shut-in period, RB was injected at 25 mL/hr and 24.2 MPa (3515 psia) for 2.0 FV to displace the fluids in the fracture volume. For the HnP cycles, membranes were placed in a core holder upstream of the HnP cell to generate the NB. Then, CO_2 and RB were simultaneously injected through the membranes at 25 mL/hr with a volumetric ratio of 90% CO_2 and 10% RB (corresponding to 22.5 mL/hr for CO_2 and 2.5 mL/hr for RB) for 2.0 FV. That is, the simultaneously injected CO_2 and RB passed through the membranes to generate the CO_2-NB before entering the HnP cell. The system was then shut-in at 31.1 MPa (4515 psia) for 13 hrs. After this shut-in period, RB was injected at 25 mL/hr and 24.2 MPa (3515 psia) to displace the fluids in the HnP cell.

To quantify the oil recovery, the total mass of the oleic and aqueous phases in each graduated cylinder was first measured. Then, the aqueous phase from each cylinder containing both phases was carefully transferred to a new cylinder. The mass of the recovered oleic phase was the difference between the mass of the graduated cylinder with (M_{oil}) and without (M_{empty}) the oleic phase. The oil recovery factor was then calculated using the mass of the recovered oleic phase, OOIP, and the density of dead oil at room temperature and atmospheric pressure (ρ_{oil}) as follows:

$$\text{oil recovery factor} = \frac{\left(\frac{M_{oil} - M_{empty}}{\rho_{oil}}\right)}{OOIP} \tag{2}$$

3. Results and Discussion

3.1. Coreflooding Experiments

Figure 5a shows the coreflooding results for BSS #1 with 5-wt% NaCl brine for 3.9 hydrocarbon pore volumes injected (HCPVI) at a constant flow rate of 4 mL/hr. The cumulative oil recovery was 36.6% OOIP with the first 33.7% being recovered before the water breakthrough at 0.34 HCPVI. Accordingly, the oil saturation in the core decreased from 65.2% to 41.4% during the injection. The pressure drop across the core increased to 68.9 kPa before the water breakthrough, then decreased to 6.89 kPa after the water breakthrough. It subsequently hovered around 55.2 kPa until the end of the injection.

Figure 5b shows the coreflooding results for BSS #2 with eCW for 8.9 HCPVI at a constant flow rate of 4 mL/hr. The cumulative oil recovery was 46.3% OOIP, where 34.3% OOIP was recovered before the breakthrough at 0.34 HCPVI. The breakthrough time was close to that in the brine case with no CO_2; however, the incremental oil recovery after the breakthrough, 11.9% OOIP, was much greater than that in the brine case. The oil saturation in the core decreased from 61.5% to 33.0% over the course of the injection. The pressure drop across the core rose to 96.5 kPa before the breakthrough, then decreased to 82.7 kPa after the breakthrough, and subsequently hovered around 96.5 kPa until the end of the injection.

Figure 5c shows the coreflooding results for BSS #3 with CO_2-NB for 7.5 HCPVI at a constant flow rate of 4 mL/hr. The cumulative oil recovery was 52.2% OOIP, where 42.8% OOIP was recovered before the breakthrough at 0.43 HCPVI. The delayed breakthrough resulted in a substantial increase in oil recovery before the breakthrough. An additional oil recovery of 9.4% OOIP was observed after the breakthrough until the end of the injection. The oil saturation in the core decreased from 61.4% to 29.3% over the course of the injection. The pressure drop across the core increased to 89.6 kPa before the breakthrough, decreased to 20.7 kPa after the breakthrough, and subsequently hovered around 96.5 kPa until the end of the injection.

Figure 6ab compares the oil recoveries from the corefloods with brine, eCW, and CO_2-NB. The oil recoveries before the breakthrough indicate that the three cases behaved like incompressible fluid displacements; that is, eCW and CO_2-NB showed no impact of CO_2 on fluid compressibility in the corefloods (Figure 6a). The brine and eCW cases showed nearly the same breakthrough time, but CO_2-NB substantially delayed the breakthrough. Consequently, the oil-recovery factor at the breakthrough (RF_{BT}) in the CO_2-NB case was 9.1% (OOIP) greater than RF_{BT} in the NaCl brine case. The substantial increase in RF_{BT} was close to the incremental oil-recovery factor by eCW, 9.7% OOIP, in comparison to the brine case after 9.0 HCPVI (Figure 6b). This highlights the importance of the enhanced RF_{BT} by the delayed breakthrough in the oil displacement by CO_2-NB.

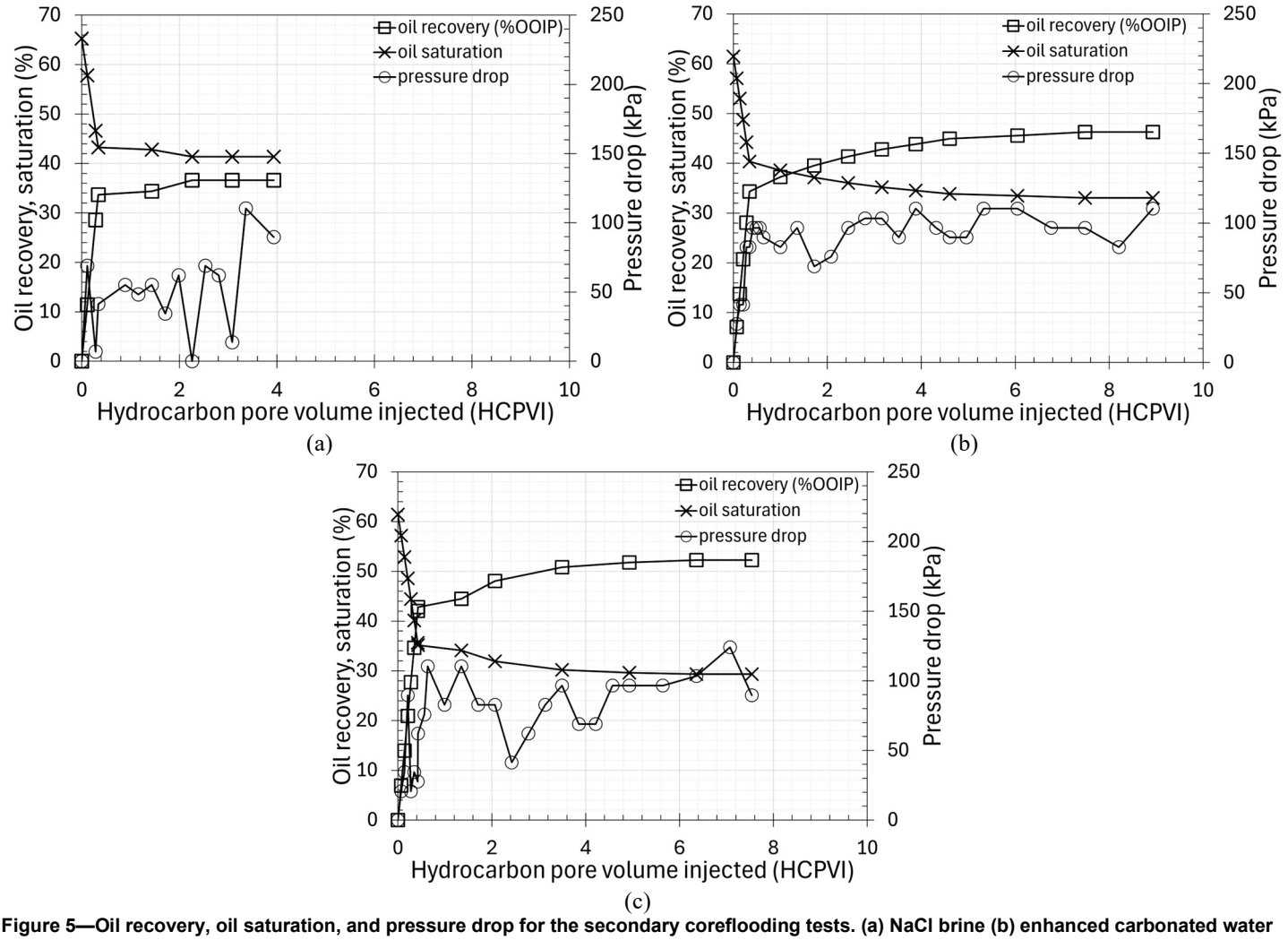

Figure 5—Oil recovery, oil saturation, and pressure drop for the secondary coreflooding tests. (a) NaCl brine (b) enhanced carbonated water (c) CO_2-nanobubble.

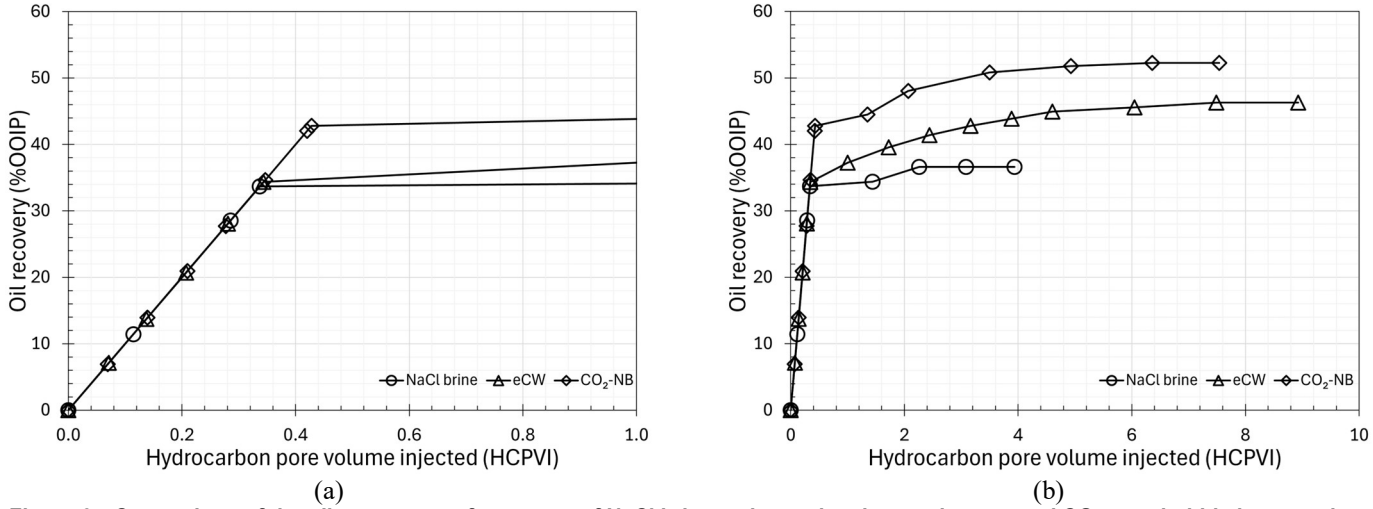

Figure 6—Comparison of the oil recovery performances of NaCl brine, enhanced carbonated water, and CO_2-nanobubble in secondary injection mode.

Figure 7 shows the calcium ion concentration in the effluent water samples measured using inductively coupled plasma mass spectrometry (ICP-MS). A greater level of calcium ions was observed with CO_2-NB than with eCW, but both cases showed significantly different behavior and greater concentrations of calcium ions than the NaCl brine case. Since the initial brine did not contain any

calcium salts, the observed calcium ion concentrations in the effluent samples came from dissolution of calcite in the cores. As discussed in the literature, this could have rendered the rock surfaces more water wet than the initial wettability; however, the impact of such wettability alteration on oil recovery was not expected to be significant with the BSS cores (Seyyedi et al. 2017). Note also that the BSS cores were not aged by oil. Nonetheless, the wettability alteration could have occurred and influenced, at least, part of the gradual increase in oil recovery factor after the breakthrough in the eCW and CO_2-NB cases (Figure 6b); however, it is unlikely to have influenced RF_{BT} that was observed only for the CO_2-NB case, not for the eCW case.

The calcite dissolution should have generated CO_2 in these experiments. Based on the calcium concentration data for the effluent samples, the amount of CO_2 generated by the calcite dissolution was estimated to be only 0.12% of the amount of CO_2 injected for the CO_2-NB case; therefore, the impact of the in-situ generated CO_2 on the oil recovery was considered negligible in these experiments.

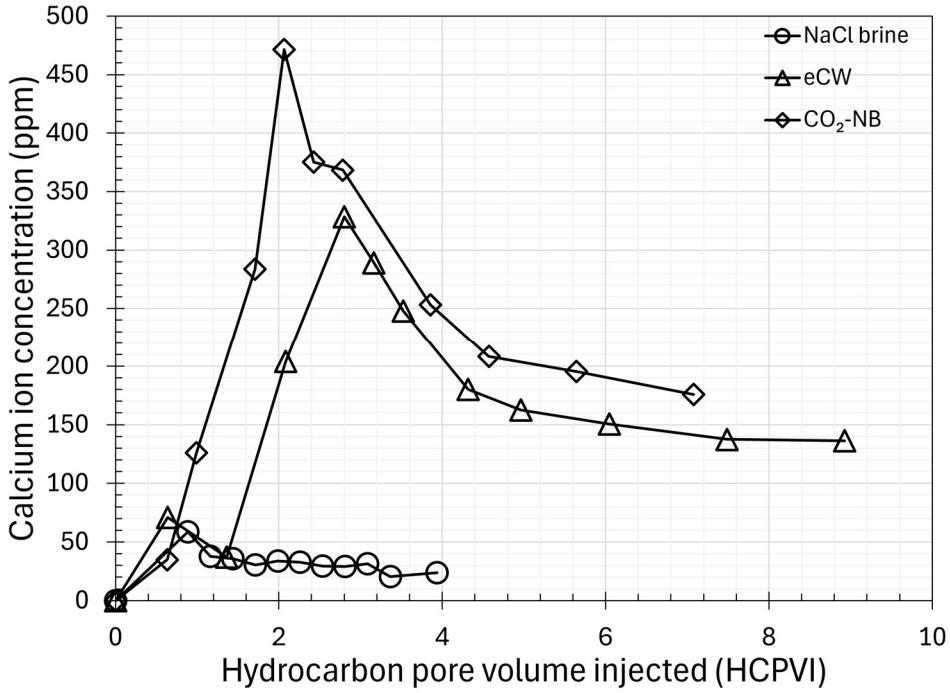

Figure 7—Calcium ion concentration measured for the effluent water samples from the secondary injection of NaCl brine, enhanced carbonated water, and CO_2-nanobubble in Berea sandstone cores.

Sohrabi et al. (2015) described possible mechanisms of EOR by CWI; e.g., enhancement in displacement efficiency through fluid/rock interactions, oil swelling, and oil viscosity reduction, and enhancement in sweep efficiency through water flow diversion. They discovered that oil recovery by CWI was substantially enhanced by formation of a new gaseous phase in addition to the aqueous and oleic phases in their high-pressure micromodel experiments. Although details of the complex interplay between phase transitions and oil displacement mechanisms are yet to be explored, their pioneering studies on CWI led to visual confirmation of the new phase during the enhanced oil displacement by CW (Seyyedi et al. 2017ab; Seyyedi and Sohrabi 2017; Seyyedi et al. 2018). Seyyed and Sohrabi (2017) concluded that the formation of a gaseous phase reduced the residual oil (the trapped oil by water) and increased the sweep efficiency by three-phase flow based on their high-pressure micromodel experiments of CWI. The impact of the gaseous phase on oil recovery was more pronounced in displacements of live oil than in those of dead oil (Sohrabi et al. 2015).

Appendix A shows the pseudo P-x diagram for the dead oil and CO_2 at 22°C as described previously. CO_2 is much more soluble in oil than in brine (see the phase boundary between L_1 and L_1-L_2); therefore, upon the contact of eCW with the resident oil in the BSS core, the CO_2 in eCW was expected to transfer to the oleic phase, as confirmed by Seyyedi et al. (2017a) for their micromodel experiments of CWI. The interphase mass transfer of CO_2 upon contact with oil should have been more pronounced in the CO_2-NB case than in the eCW case because the former involved a higher level of supersaturation of the aqueous phase by CO_2 and dispersion of CO_2 nanobubbles as a CO_2 buffer (Wang et al. 2023; Achour et al. 2024). Such mass transfer of an EOR agent is somewhat analogous to the solvent mass transfer in EOR with aqueous solution of oxygenated solvent, such as ketone and ether (e.g., Wang et al. 2020; Lawal et al. 2022, 2024).

Sohrabi et al. (2015) compared high-pressure micromodel experiments of live oil displacements by water and CW. Their CW injection yielded 10% greater RF_{BT} than the water injection. The comparative experiments of dead-oil displacements by water and CW did not show such a delayed breakthrough and an enhanced RF_{BT}. Interestingly, RF_{BT} with eCW and CO_2-NB in Figure 6 behaved similarly to the live oil experiments with water and CW in Sohrabi et al. (2015). The similarity was likely related to the amount of gaseous species, including CO_2, that contributed to the nucleation of a gaseous phase. The occurrence of an enhanced RF_{BT} [i.e., CO_2-NB in Figure 6 and CW with live oil in Sohrabi et al. (2015)] was likely related to the competition between the interphase mass transfer of the gaseous species and the local mixing/equilibrium process near the interface during the oil displacement. The pseudo P-x diagram in Appendix A indicates that L_1-L_2 requires over 80 mol% of CO_2 at the experimental pressure and temperature. Such high concentrations of CO_2 are conceivable locally near the displacement fronts where the metastable aqueous phase (CO_2-NB) releases CO_2 to the oleic phase while the nanobubbles of CO_2 with capillary pressure release CO_2 to the surrounding aqueous phase. The in-situ formation of the L_2 phase should have been much more significant with CO_2-NB than with eCW, leading to the marked difference in RF_{BT}.

It is reasonable to consider that the oil displacements by eCW and CO_2-NB involved three phases: the aqueous (W), oleic (L_1), and CO_2-rich liquid (L_2) phases. LaForce and Orr (2009) studied simultaneous water-gas injection for one-dimensional oil displacements with varying water-gas ratios using the method of characteristics (MOC). Their MOC solutions involved three-phase displacements of W, L_1, and L_2 in quaternary systems of water, CO_2, and two hydrocarbon components. One of their important findings was that multicontact miscibility (MCM) can be developed through W-L_1-L_2 three-phase flow if the concentration of CO_2 in the injection fluid is large enough so that the mobility of the L_2 phase can exceed that of the W phase. Such a gas concentration in the injection fluid was referred to as the minimum gas fraction (MGF). LaForce and Orr (2009) concluded that the MGF was sensitive to phase behavior and gas/water relative permeability.

One of the example solutions in LaForce and Orr (2009) was presented for simultaneous CO_2-water injection for oil displacement below the MMP between oil and CO_2 in a quaternary system of water, methane, CO_2, and C_{10}. The injection composition varied from pure water to mixtures of CO_2 and water with increasing CO_2 concentration. The initial oil consisted of methane and C_{10}. That example solution was quite useful for the interpretation of the corefloods in this research since these corefloods were below the MMP as shown in Appendix A. Comparison between two injection compositions below and above the MGF in LaForce and Orr (2009) showed a clear difference near the displacement front; that is, the CO_2 concentration above the MGF yielded a partially miscible displacement of C_{10} by a CO_2 bank followed by a water bank, while the CO_2 concentration below the MGF yielded an immiscible displacement of C_{10} by a water bank followed by a small CO_2 bank. The oil displacement front in the former was substantially delayed in comparison to that in the latter, as observed in the CO_2-NB case in comparison to the eCW case in this research. Also, the pure water injection and a CO_2 concentration below the MGF in LaForce and Orr (2009) showed only differences caused by a slow-moving small CO_2 bank behind the water bank. This may explain the gradual increase in oil recovery factor after the breakthrough in the eCW case in comparison to the brine case in this research.

Note, however, that corefloods always involve three-dimensional flow under micro- and core-scale heterogeneity of petrophysical properties. The example solutions for 1-D convective flow with no dispersion in a quaternary system (LaForce and Orr 2009) are not expected to fully represent complex mechanisms in the corefloods in this research. For example, it is conceivable that the competition between CO_2 and water in multiphase fractional flow occurred differently in different hydraulic paths in the BSS cores, and they collectively affected the oil recovery characteristics.

3.2. Huff-n-Puff Experiments

Set 1 – Annular Fracture.

Figure 8 shows the oil recovery results of the CO_2/RB HnP experiments for set 1 with and without NB. For the CO_2-RB (without NB) experiment, the cumulative oil recovery after four cycles was 24% OOIP. The 1st co-injection cycle yielded 15.7% oil recovery, followed by 5.1% from the 2nd cycle, 1.7% from the 3rd cycle, and 1.5% from the 4th cycle. The 1st cycle yielded the largest oil recovery and the incremental oil recovery decreased for each subsequent CO_2/RB co-injection cycle.

The CO_2-NB (with NB) experiment yielded a similar trend with a larger cumulative oil recovery of 34.4% OOIP after four cycles. The 1st co-injection cycle yielded 23.8% oil recovery, followed by 5.8% from the 2nd cycle, 3.3% from the 3rd cycle, and 1.6% from the 4th cycle. Overall, for the CO_2/RB co-injection cycles, the case with NB resulted in a 10.4% increase in improved oil recovery. The concentration of CO_2 in the produced oil sample (at ambient conditions) was determined to be negligible (approximately 1 mol%)

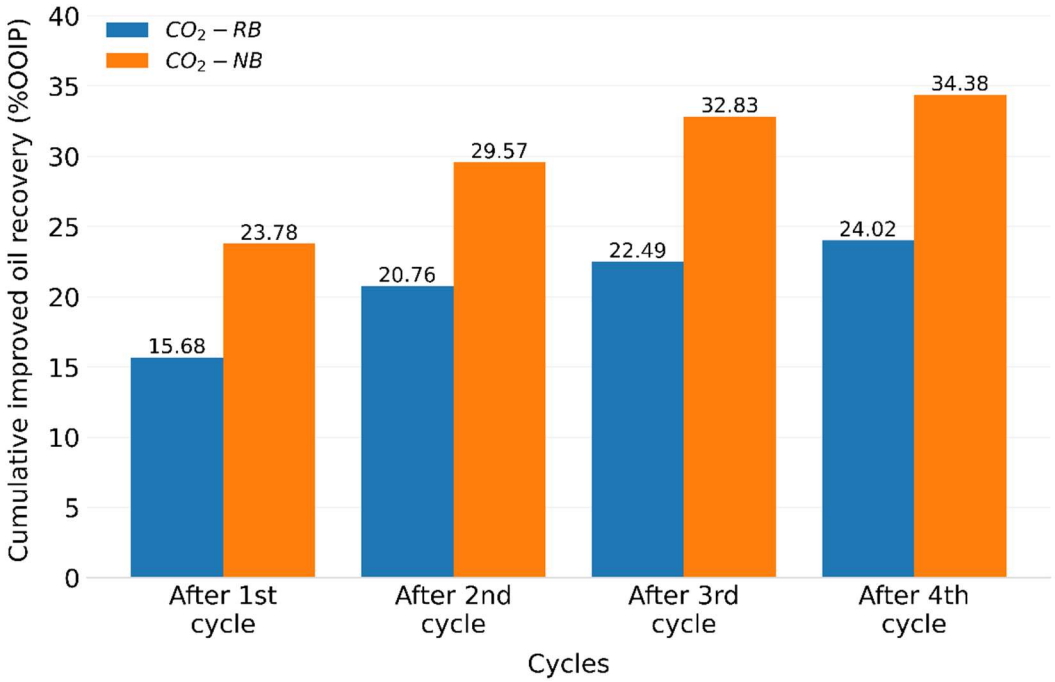

Figure 8—Cumulative improved oil recovery for the CO_2/RB HnP experiments with and without NB (Set 1).

Figure 9 further shows the cumulative oil recovery (%OOIP) for set 1, including the oil recovery from the RB flooding stage. Set 1 with NB yielded an overall cumulative oil recovery of 60.7% OOIP while set 1 without NB yielded an overall cumulative oil recovery of 47.5%.

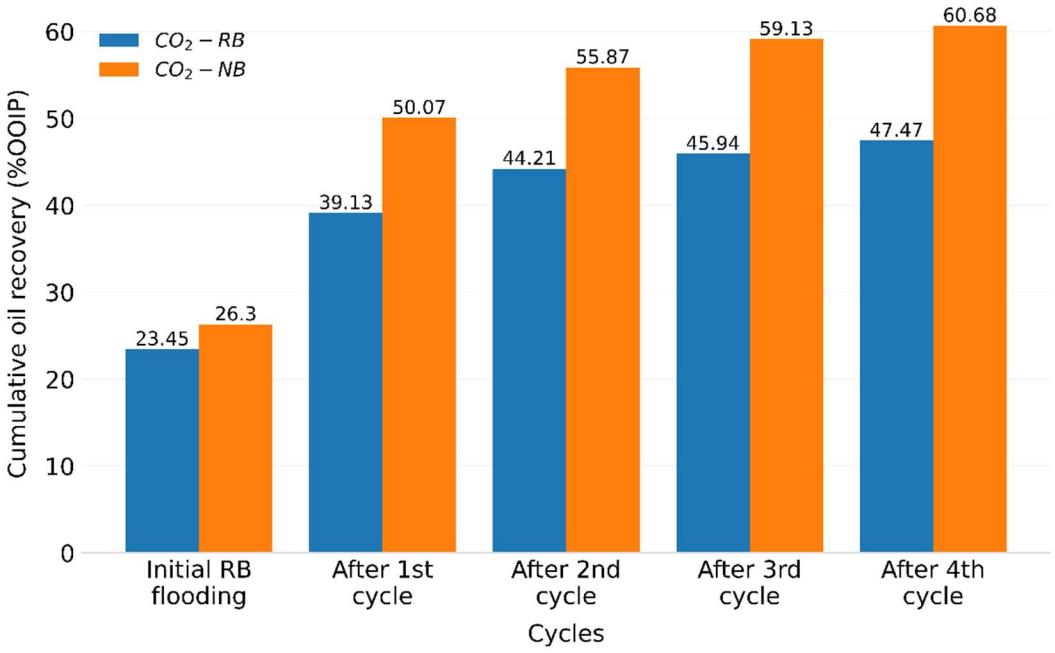

Figure 9—Cumulative oil recovery for the CO_2/RB HnP experiments with and without NB including the initial RB flooding stage (Set 1).

Set 2 – Artificial Fracture.

Figure 10 shows the oil recovery results of the CO_2/RB HnP experiments for set 2 with and without NB. For the CO_2-RB experiment, the cumulative oil recovery was 22.1% OOIP after 2 cycles of co-injection. The 1st co-injection cycle yielded 15.6% oil recovery while the 2nd cycle yielded 6.5% oil recovery. For the CO_2-NB experiment, the cumulative oil recovery for the CO_2/RB co-injection after 2 cycles was 36.2% OOIP (23.5% coming from the 1st co-injection cycle and 12.7% from the 2nd cycle).

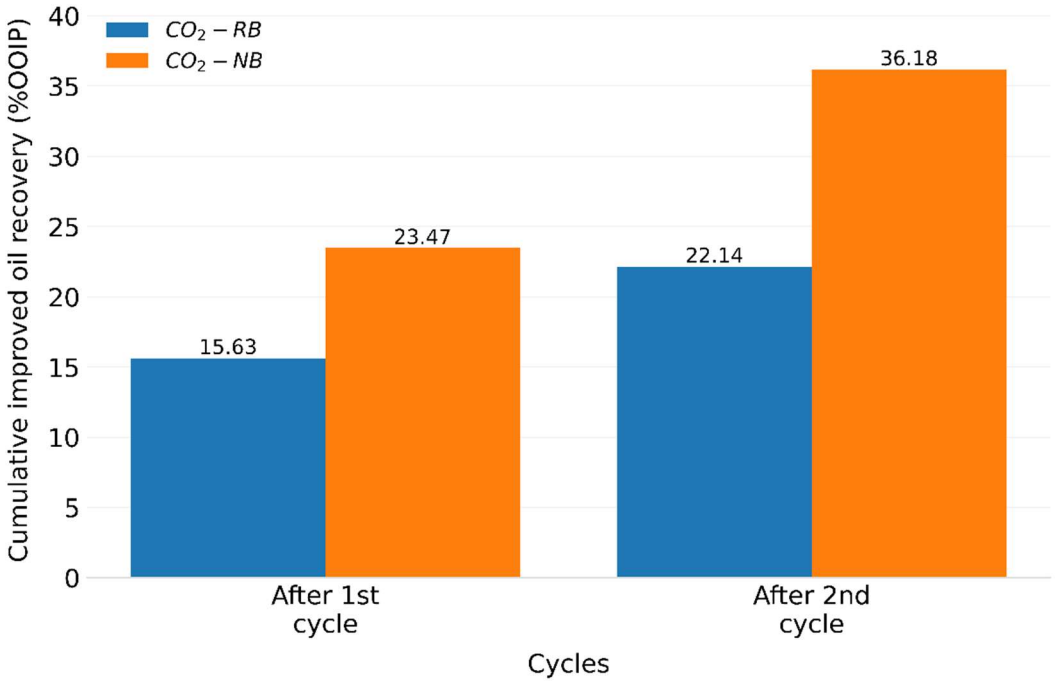

Figure 10—Cumulative improved oil recovery for the CO_2/RB HnP experiments with and without NB (Set 2).

The HnP in set 2 was limited to only 2 CO_2/RB co-injection cycles because precipitates, caused by the reaction of CO_2 with brine, formed in the inlet holes of the core holder housing the cores and the NB membranes. Overall, for the CO_2/RB co-injection cycles, the case with NB resulted in a 14.0% increase in improved oil recovery. Additional cycles would likely have led to an increase in improved oil recovery.

Figure 11 shows the cumulative oil recovery (%OOIP) for set 2, including the oil recovery from the RB flooding stage. Set 2 with NB yielded an overall cumulative oil recovery of 48.3% OOIP while Set 2 without NB yielded an overall cumulative oil recovery of 36.3%.

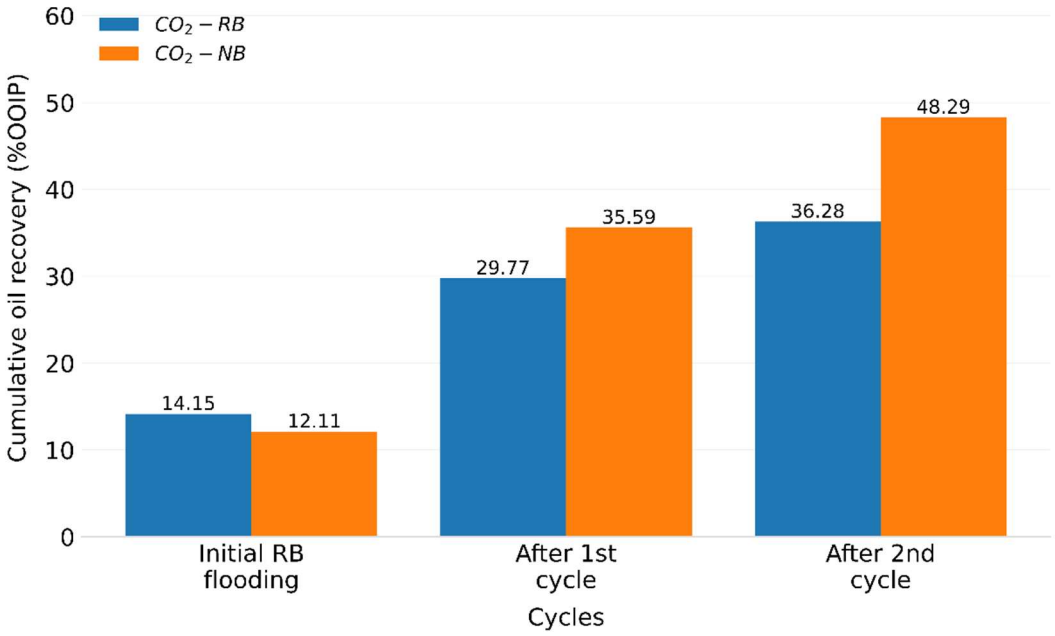

Figure 11—Cumulative oil recovery for the CO_2/RB HnP experiments with and without NB including the initial RB flooding stage (Set 2).

Set 3 – Annular + Artificial Fracture.

Figure 12 shows the oil recovery results of the CO_2/RB HnP experiments for set 3, with and without NB. For the CO_2-RB experiment, the cumulative oil recovery for the CO_2/RB co-injection after four cycles was 28.1% OOIP. The 1st co-injection cycle yielded 15.3% oil

recovery, followed by 7.4% from the 2nd cycle, 3.2% from the 3rd cycle, and 2.2% from the 4th cycle. For the CO_2-NB experiment, the huff-n-puff was limited to only three cycles due to the formation of CO_2-RB precipitates in the core holder housing the NB membranes. The cumulative oil recovery for the CO_2/RB co-injection after three cycles was 52.9% OOIP. The 1st cycle yielded 30.2% oil recovery, followed by 5.0% oil recovery from the 2nd cycle, and 4.0% oil recovery from the 3rd cycle. This trend shows that a 4th cycle would likely have yielded some more oil recovery. Overall, for the CO_2/RB co-injection cycles, the case with NB resulted in an 11.1% increase in improved oil recovery.

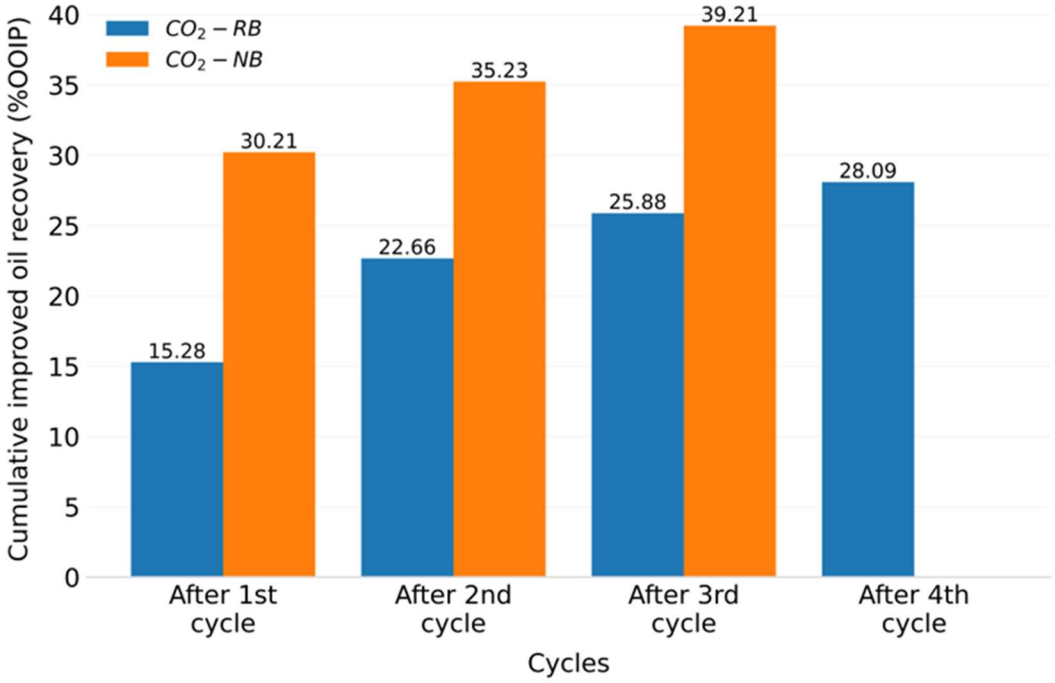

Figure 12—Cumulative improved oil recovery for the CO_2/RB HnP experiments with and without NB (Set 3).

Figure 13 shows the cumulative oil recovery (% OOIP) for set 3, including the oil recovery from the RB flooding stage. Set 3 with NB yielded an overall cumulative oil recovery of 52.9% OOIP while set 3 without NB yielded an overall cumulative oil recovery of 51.6%. The initial RB flooding stage yielded 13.7% oil recovery for set 3 with NB compared to 23.5% oil recovery for set 3 without NB. At the moment, it is not clear what caused this difference in oil recovery from the initial RB flooding stage for set 3.

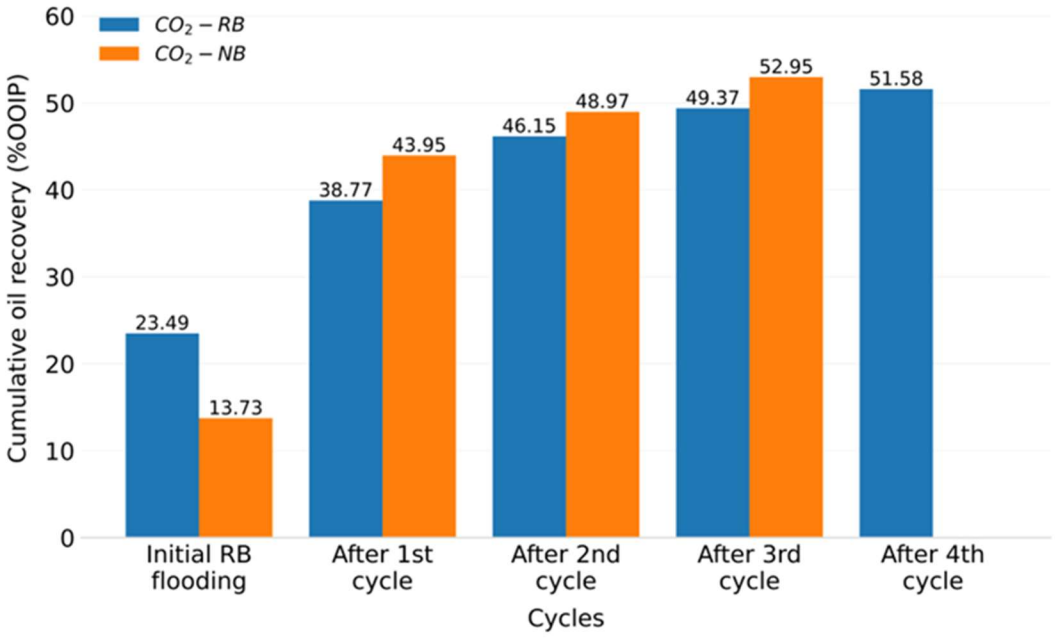

Figure 13—Cumulative oil recovery for the CO_2/RB HnP experiments with and without NB including the initial RB flooding stage (Set 3).

Figure 14 shows the cumulative improved oil recovery for all three sets–with and without NB–after several HnP cycles. For set 1, CO_2-NB recovered 34.4% OOIP while CO_2-RB (without NB) recovered 24.0% OOIP through four HnP cycles. For set 2, only two HnP cycles were performed. CO_2-NB recovered 36.2% OOIP while CO_2-RB recovered 22.1% OOIP. For set 3, three HnP cycles were performed for the CO_2-NB case while four HnP cycles were performed for the CO_2-RB case. The CO_2-RB case recovered 28.1% OOIP; this was 11.1% less than the 39.2% OOIP recovered from the CO_2-NB case, although it had one more HnP cycle than the CO_2-NB case. Figure 14 shows systematically greater oil recoveries with CO_2-NB than CO_2-RB, highlighting the enhanced oil recovery by CO_2-NB.

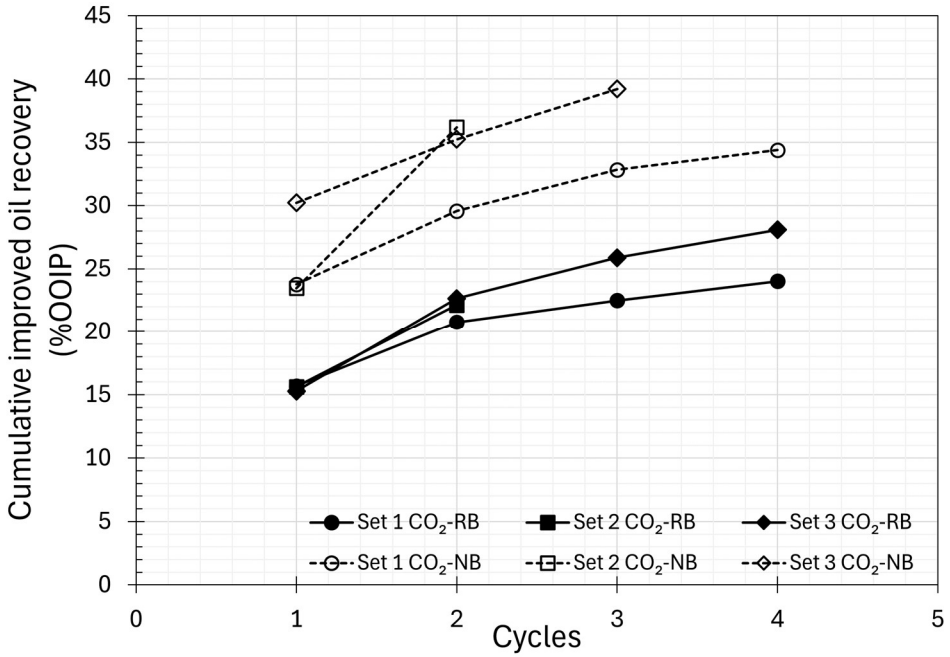

Figure 14—Cumulative improved oil recovery for the CO_2/RB huff-n-puff experiments with and without NB (Sets 1 – 3). Four CO_2 huff-n-puff cycles were conducted for set 1. Two huff-n-puff cycles were conducted for set 2. For set 3, four huff-n-puff cycles were conducted for the case without NB while only three cycles were conducted for the case with NB.

Figure 15 shows cumulative oil recovery for each HnP cycle with respect to surface area per unit volume, λ^{-1}. For the three sets (with and without NB), there is little variation in cumulative improved oil recovery as λ^{-1} changes. The cumulative oil recoveries ranged from 34.4% to 39.2% OOIP for the sets with NB while the oil recoveries ranged from 22.1% to 28.1% OOIP for the CO_2-RB sets. Set 2 had only two HnP cycles; therefore, additional cycles could have led to greater oil recoveries for the sets with and without NB. Likewise, a 4th HnP cycle for CO_2-NB in set 3 could have led to a higher improved oil recovery.

An interesting point to note in the sets with CO_2-NB is that sets 2 and 3 with artificial fracture (set 3 had a combination of artificial and annular fractures) had greater improved oil recoveries than set 1 with only the annular fracture. It is likely that the presence of an artificial fracture matrix configuration contributed most to oil recovery performance in HnP. A similar trend could have been observed in the sets with CO_2-RB, if set 2 had undergone more HnP cycles. Nevertheless, the variability in improved oil recovery among sets 1, 2, and 3 is less than that between the improved oil recovery from the CO_2-RB and CO_2-NB cases.

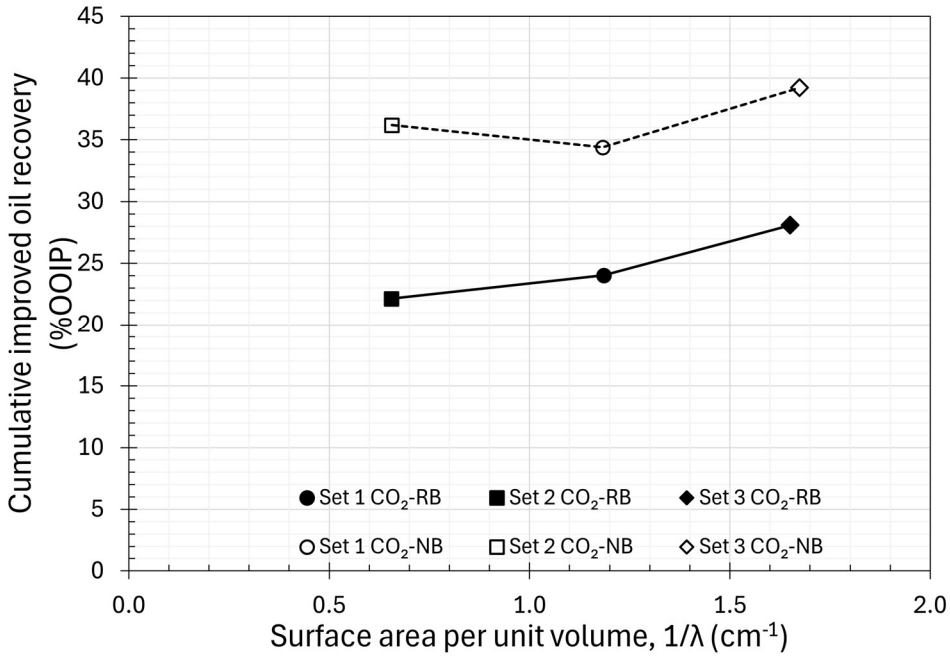

Figure 15—Cumulative improved oil recovery per λ^{-1} (Sets 1 – 3). Set 1 underwent four CO_2 huff-n-puff cycles, set 2 underwent two huff-n-puff cycles, set 3 underwent four huff-n-puff cycles without NB and three cycles with NB.

4. Conclusions

This paper presented an experimental study of aqueous nanobubble dispersion of CO_2 (CO_2-NB) for enhanced oil recovery. CO_2-NB was compared with brine and slightly supersaturated carbonated water (eCW) in corefloods with Berea sandstone cores and dead oil at room temperature. CO_2-NB was also compared with a mixture of CO_2 and brine with no NB in high-pressure high-temperature huff-n-puff experiments with live oil-saturated tight Kentucky sandstone cores using three different fracture-matrix configurations. The main conclusions are as follows:

1. Coreflooding results showed that the displacement of oil by CO_2-NB yielded a delayed breakthrough with the oil recovery factor at breakthrough (RF_{BT}) that was 9.1% OOIP greater than RF_{BT} in the brine case. The displacement of oil by eCW did not show such an increase in RF_{BT}, but showed a long-term gradual increase in oil recovery after the breakthrough. The increased RF_{BT} by CO_2-NB can be attributed to the nucleation of a CO_2-rich phase near the displacement fronts, where the metastable aqueous phase releases CO_2 to the oleic phase while the nanobubbles of CO_2 with capillary pressure release CO_2 to the surrounding aqueous phase. That is, the partially miscible displacement of dead oil by the in-situ generated CO_2-rich phase could have enhanced RF_{BT} by CO_2-NB in comparison to the immiscible oil displacement by water in the brine case.

2. Corefloods with CO_2-NB and eCW showed an elevated level of calcite dissolution in comparison to the brine case. Wettability alteration could have caused part of the incremental oil recovery observed for the CO_2-NB and eCW cases, among several other factors, such as oil swelling and oil viscosity reduction.

3. Huff-n-puff experiments showed a systematic increase in oil recovery with CO_2-NB than with CO_2-RB (with no NB) for three different fracture-matrix configurations. The difference in improved oil recovery among the different fracture-matrix configurations tested was smaller than the difference between the CO_2-NB and CO_2-RB cases.

Acknowledgments

We gratefully acknowledge the sponsors of the Energi Simulation Industrial Affiliate Program on Carbon Utilization and Storage (ES Carbon UT) at the University of Texas at Austin. Ryosuke Okuno holds the Pioneer Corporation Faculty Fellowship in Petroleum Engineering at the University of Texas at Austin.

References

Achour, S.H., Lawal, T., Sheng, K., and Okuno, R. 2024. Thermodynamic Modeling of Aqueous Nanobubble Dispersion. Accepted for publication in *SPE Journal,* January 31, 2024. https://doi.org/10.2118/215122-PA.

Ahmadi, K., and Johns, R.T. 2011. Multiple-Mixing-Cell Method for MMP Calculations, *SPE Journal* **16**(4): 733-742. https://doi.org/10.2118/116823-PA.

Ahmed, A.K.A., Sun, C., Hua, L., et al. 2018. Generation of Nanobubbles by Ceramic Membrane Filters: The Dependence of Bubble Size and Zeta Potential on Surface Coating, Pore Size and Injected Gas Pressure. *Chemosphere* **203**: 327–35. https://doi.org/10.1016/j.chemosphere.2018.03.157.

Atkinson, A.J., Apul, O.G., Schneider, O., et al. 2019. Nanobubble Technologies Offer Opportunities To Improve Water Treatment. *Accounts of Chemical Research* **52**(5): 1196–1205. https://doi.org/10.1021/acs.accounts.8b00606.

Chen, Y., Sari, A., Xie, Q., et al. 2019. Insights into the Wettability Alteration of CO_2-Assisted EOR in Carbonate Reservoirs. *Journal of Molecular Liquids* **279**: 420–26. https://doi.org/10.1016/j.molliq.2019.01.112.

Drexler, S., Hoerlle, F., Godoy, W., et al. 2020. Wettability Alteration by Carbonated Brine Injection and Its Impact on Pore-Scale Multiphase Flow for Carbon Capture and Storage and Enhanced Oil Recovery in a Carbonate Reservoir. *Applied Sciences* **10**(18): 6496. https://doi.org/10.3390/app10186496.

Duan, Z., and Sun, R. 2003. An Improved Model Calculating CO_2 Solubility in Pure Water and Aqueous NaCl Solutions from 273 to 533 K and from 0 to 2000 Bar. *Chemical Geology* **193**(3–4): 257–71. https://doi.org/10.1016/S0009-2541(02)00263-2.

Ebina, K., Shi, K., Hirao, M., et al. 2013. Oxygen and Air Nanobubble Water Solution Promote the Growth of Plants, Fishes, and Mice. Edited by Jose Luis Balcazar. *PLoS ONE* **8**(6): e65339. https://doi.org/10.1371/journal.pone.0065339.

Favvas, E.P., Kyzas, G.Z., Efthimiadou, E.K., et al. 2021. Bulk Nanobubbles, Generation Methods and Potential Applications. *Current Opinion in Colloid & Interface Science* **54**: 101455. https://doi.org/10.1016/j.cocis.2021.101455.

Ghandi, E., Parsaei, R., and Riazi, M. 2019. Enhancing the Spontaneous Imbibition Rate of Water in Oil-Wet Dolomite Rocks through Boosting a Wettability Alteration Process Using Carbonated Smart Brines. *Petroleum Science* **16**(6): 1361–73. https://doi.org/10.1007/s12182-019-0355-1.

Ghosh, B., Kilybay, A., Thomas, N.C., et al. 2022. Hybrid Carbonated Engineered Water as EOR Solution for Oil-Wet Carbonate Formation. *Energies* **15**(21): 7889. https://doi.org/10.3390/en15217889.

Grape, S.G., Poston, S.W., and Osoba, J.S. 1990. Imbibition Flooding with CO_2-Enriched Water. Paper presented at the International Symposium of the Society of Core Analysts.

Hernandez-Aguilar, J.R., Cunningham, R., and Finch, J.A. 2006. A Test of the Tate Equation to Predict Bubble Size at an Orifice in the Presence of Frother. *International Journal of Mineral Processing* **79**(2): 89–97. https://doi.org/10.1016/j.minpro.2005.12.003.

Jadhav, A.J., and Barigou, M. 2020. Bulk Nanobubbles or Not Nanobubbles: That Is the Question. *Langmuir* **36**(7): 1699–1708. https://doi.org/10.1021/acs.langmuir.9b03532.

Kechut, N.I.I., Riazi, M., Sohrabi, M., et al. 2010. Tertiary Oil Recovery and CO_2 Sequestration by Carbonated Water Injection (CWI). Paper presented at the SPE International Conference on CO_2 Capture, Storage, and Utilization, New Orleans, Louisiana, USA, 10 – 12 November. SPE-139667-MS. https://doi.org/10.2118/139667-MS.

Kikuchi, K., Tanaka, Y., Saihara, Y., et al. 2006. Concentration of Hydrogen Nanobubbles in Electrolyzed Water. *Journal of Colloid and Interface Science* **298**(2): 914–19. https://doi.org/10.1016/j.jcis.2006.01.010.

Kikuchi, K., Nagata, S., Tanaka, Y., et al. 2007. Characteristics of Hydrogen Nanobubbles in Solutions Obtained with Water Electrolysis. *Journal of Electroanalytical Chemistry* **600**(2): 303–10. https://doi.org/10.1016/j.jelechem.2006.10.005.

Kikuchi, K., Ioka, A., Oku, T., et al. 2009. Concentration Determination of Oxygen Nanobubbles in Electrolyzed Water. *Journal of Colloid and Interface Science* **329**(2): 306–9. https://doi.org/10.1016/j.jcis.2008.10.009.

Kukizaki, M., and Goto, M. 2006. Size Control of Nanobubbles Generated from Shirasu-Porous-Glass (SPG) Membranes. *Journal of Membrane Science* **281**(1–2): 386–96. https://doi.org/10.1016/j.memsci.2006.04.007.

Kumar, A. and Okuno, R. 2016. A New Algorithm for Multiphase Fluid Characterization for Solvent Injection. *SPE Journal* **21**(5): 1688 – 1704. http://dx.doi.org/10.2118/175123-PA

LaForce, T., and Orr, F.M. 2009. Four-Component Gas/Water/Oil Displacements in One Dimension: Part III, Development of Miscibility. *Transport in Porous Media* **79**(2): 225–47. https://doi.org/10.1007/s11242-008-9311-z.

Lawal, T., Wang, M., Abeykoon, G.A., et al. 2022. Effect of Chemical Partition Behavior on Oil Recovery by Wettability Alteration in Fractured Tight Reservoirs. *Energy & Fuels* **36**(2): 797–805. https://doi.org/10.1021/acs.energyfuels.1c03344.

Lawal, T., Mirzaei-Paiaman, A., and Okuno, R. 2024. Aqueous Ketone Solution for Wettability Alteration in High-salinity-high-temperature Carbonate Reservoirs. Paper presented at the SPE Improved Oil Recovery Conference, Tulsa, Oklahoma, USA, 23 – 25 April. SPE-218246-MS.

Li, L., Khorsandi, S., Johns, R.T. Ahmadi, K. 2015. Multiple-Mixing-Cell Method for Three-Hydrocarbon-Phase Displacements. *SPE Journal* **20**(6): 1339-1349. https://doi.org/10.2118/169150-PA.

Lyu, T., Wu, S., Mortimer, R.J.G., et al. 2019. Nanobubble Technology in Environmental Engineering: Revolutionization Potential and Challenges. *Environmental Science & Technology* **53**(13): 7175–76. https://doi.org/10.1021/acs.est.9b02821.

Oh, S.H., and Kim, J.-M. 2017. Generation and Stability of Bulk Nanobubbles. *Langmuir* **33**(15): 3818–23. https://doi.org/10.1021/acs.langmuir.7b00510.

Ohgaki, K., Khanh, N.Q., Joden, Y., et al. 2010. Physicochemical Approach to Nanobubble Solutions. *Chemical Engineering Science* **65**(3): 1296–1300. https://doi.org/10.1016/j.ces.2009.10.003.

Okuno, R., Johns, R.T., and Sepehrnoori, K. 2011. Mechanisms for High Displacement Efficiency of Low-Temperature CO_2 Floods, *SPE Journal* **16**(4): 751-767. http://dx.doi.org/10.2118/129846-PA

Okuno, R. and Xu, Z. 2014. Mass Transfer on Multiphase Transitions in Low-Temperature Carbon-Dioxide Floods. *SPE Journal* **19**(6): 1005-1023. http://dx.doi.org/10.2118/166345-PA

Oliveira, H., Azevedo, A., and Rubio, J. 2018. Nanobubbles Generation in a High-Rate Hydrodynamic Cavitation Tube. *Minerals Engineering* **116**: 32–34. https://doi.org/10.1016/j.mineng.2017.10.020.

Pal, P., Joshi, A., and Anantharaman, H. 2022. Nanobubble Ozonation for Waterbody Rejuvenation at Different Locations in India: A Holistic and Sustainable Approach. *Results in Engineering* **16**: 100725. https://doi.org/10.1016/j.rineng.2022.100725.

Parkhurst, D.L., and Appelo, C.A.J. 2013. Description of Input and Examples for PHREEQC Version 3–A Computer Program for Speciation, Batch-Reaction, One-Dimensional Transport, and Inverse Geochemical Calculations: U.S. Geological Survey Techniques and Methods, United States Geological Survey (USGS). https://pubs.usgs.gov/tm/06/a43/.

Perez, J.M. 1992. Carbonated Water Imbibition Flooding: An Enhanced Oil Recovery Process for Fractured Reservoirs, Paper presented at the SPE/DOE Eight Symposium on Enhanced Oil Recovery, Tulsa, Oklahoma, 22 – 24 April. SPE/DOE-24164.

Perez Sirkin, Y.A., Gadea, E.D., Scherlis, D.A., et al. 2019. Mechanisms of Nucleation and Stationary States of Electrochemically Generated Nanobubbles. *Journal of the American Chemical Society* **141**(27): 10801–11. https://doi.org/10.1021/jacs.9b04479.

Riazi, M., Sohrabi, M., Jamiolahmady, M., et al. 2009. Oil Recovery Improvement Using CO_2-Enriched Water Injection. Paper presented at the SPE EUROPEC/EAGE Annual Conference and Exhibition, Amsterdam, The Netherlands, 8 – 11 June. SPE-121170-MS. https://doi.org/10.2118/121170-MS.

Ruidiaz, E.M., Winter, A., and Trevisan, O.V. 2018. Oil Recovery and Wettability Alteration in Carbonates Due to Carbonate Water Injection. *Journal of Petroleum Exploration and Production Technology* **8**(1): 249–58. https://doi.org/10.1007/s13202-017-0345-z.

Seyyedi, M., Sohrabi, M., and Farzaneh, A. 2015. Investigation of Rock Wettability Alteration by Carbonated Water through Contact Angle Measurements. *Energy & Fuels* **29**(9): 5544–53. https://doi.org/10.1021/acs.energyfuels.5b01069.

Seyyedi, M., and Sohrabi, M. 2016. Enhancing Water Imbibition Rate and Oil Recovery by Carbonated Water in Carbonate and Sandstone Rocks. *Energy & Fuels* **30**(1): 285–93. https://doi.org/10.1021/acs.energyfuels.5b02644.

Seyyedi, M., and Sohrabi, M. 2017. Pore-Scale Investigation of Crude Oil/CO_2 Compositional Effects on Oil Recovery by Carbonated Water Injection. *Industrial & Engineering Chemistry Research* **56**(6): 1671–81. https://doi.org/10.1021/acs.iecr.6b04743.

Seyyedi, M., Mahzari, P., and Sohrabi, M. 2017a. An Integrated Study of the Dominant Mechanism Leading to Improved Oil Recovery by Carbonated Water Injection. *Journal of Industrial and Engineering Chemistry* **45**: 22–32. https://doi.org/10.1016/j.jiec.2016.08.027.

Seyyedi, M., Sohrabi, M., and Sisson, A. 2017b. Experimental Investigation of the Coupling Impacts of New Gaseous Phase Formation and Wettability Alteration on Improved Oil Recovery by CWI. *Journal of Petroleum Science and Engineering* **150**: 99–107. https://doi.org/10.1016/j.petrol.2016.11.016.

Seyyedi, M., Mahzari, P., and Sohrabi, M. 2018. A Comparative Study of Oil Compositional Variations during CO_2 and Carbonated Water Injection Scenarios for EOR. *Journal of Petroleum Science and Engineering* **164**: 685–95. https://doi.org/10.1016/j.petrol.2018.01.029.

Smirnov, B.M., and Berry, R.S. 2015. Growth of Bubbles in Liquid. *Chemistry Central Journal* **9**(1): 48. https://doi.org/10.1186/s13065-015-0127-y.

Sohrabi, M., Kechut, N.I., Riazi, M., et al. 2011. Safe Storage of CO_2 Together with Improved Oil Recovery by CO_2-Enriched Water Injection. *Chemical Engineering Research and Design*, Special Issue on Carbon Capture & Storage, **89**(9): 1865–72. https://doi.org/10.1016/j.cherd.2011.01.027.

Sohrabi, M., Emadi, A., Farzaneh, S.A., et al. 2015. A Thorough Investigation of Mechanisms of Enhanced Oil Recovery by Carbonated Water Injection. Paper presented at the SPE Annual Technical Conference and Exhibition, Houston, Texas, USA, 28 – 30 September. SPE-175159-MS. https://doi.org/10.2118/175159-MS.

Temesgen, T., Bui, T.T., Han, M., et al. 2017. Micro and Nanobubble Technologies as a New Horizon for Water-Treatment Techniques: A Review. *Advances in Colloid and Interface Science* **246**: 40–51. https://doi.org/10.1016/j.cis.2017.06.011.

Ulatowski, K., Sobieszuk, P., Mróz, A., et al. 2019. Stability of Nanobubbles Generated in Water Using Porous Membrane System. *Chemical Engineering and Processing - Process Intensification* **136**: 62–71. https://doi.org/10.1016/j.cep.2018.12.010.

Vadhan, R.S., and Phukan, R. 2022. Carbonated Smart Water Injection for Enhanced Oil Recovery in Sandstone Reservoirs of Upper Assam Basin, India. Paper presented at the EAGE Annual Conference and Exhibition, Madrid, Spain, 6 – 9 June. SPE-209671-MS. https://doi.org/10.2118/209671-MS.

Wang, M., Abeykoon, G.A., Argüelles-Vivas, F.J., et al. 2020. Aqueous Solution of Ketone Solvent for Enhanced Water Imbibition in Fractured Carbonate Reservoirs. *SPE Journal* **25**(5): 2694–2709. https://doi.org/10.2118/200340-PA.

Wang, H., Lawal, T., Achour, S.H., et al. 2023. Aqueous Nanobubble Dispersion of CO_2 at Pressures Up To 208 Bara. *Energy & Fuels* **37**(24): 19726–37. https://doi.org/10.1021/acs.energyfuels.3c03660.

Wang, H., Carrasco-Jaim, O., and Okuno, R. 2024. Aqueous Nanobubble Dispersion of CO_2 in Sodium Formate Solution for Enhanced CO_2 Mineralization Using Basaltic Rocks. Paper presented at the Carbon Capture, Utilization, and Storage Conference, Houston, Texas, 11 – 13 March.

Zhang, X., Wei, B., Shang, J., et al. 2018. Alterations of Geochemical Properties of a Tight Sandstone Reservoir Caused by Supercritical CO_2-Brine-Rock Interactions in CO_2-EOR and Geosequestration. *Journal of CO_2 Utilization* **28**: 408–18. https://doi.org/10.1016/j.jcou.2018.11.002.

Zhu, J., An, H., Alheshibri, M., et al. 2016. Cleaning with Bulk Nanobubbles. *Langmuir* **32**(43): 11203–11. https://doi.org/10.1021/acs.langmuir.6b01004.

Appendix A—Fluid Properties and Models

This appendix summarizes the properties and models for the fluids used in the research. The data and models in this section include the dead oil and live oil EOS models.

A Peng-Robinson EOS model was calibrated for the CO_2/dead oil and CO_2/live oil mixtures using PVT data including constant mass expansion, swelling tests, and densities measured at different conditions. Figure A-1 shows the simulated P-x diagram for the pseudo-binary of CO_2 and dead oil.

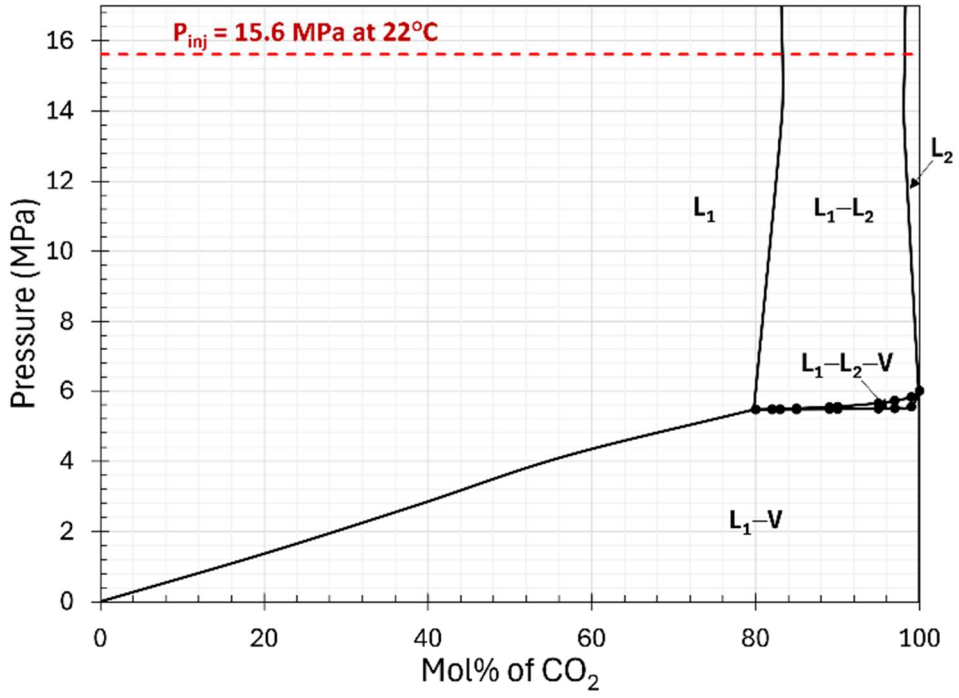

Figure A-1— P-x diagram of CO_2 and the dead oil based on the calibrated EOS model.

Tables A-1 and A-2 show the parameters of the calibrated Peng-Robinson EOS model for the live oil/CO_2 mixtures and the corresponding binary interaction parameters. Figure A-2 shows the swelling test data for the pseudo-binary of CO_2 and live oil.

Table A-1—Parameters of the calibrated Peng Robinson EOS model for the live oil used in this research. "PC" stands for pseudo component.

Components	Mol. %	MW (g/mol)	T_c (°C)	P_c (MPa)	Acentric factor	Volume shift (mL/mol)
CO_2	1.76E-5	44.010	31.050	7.376	0.2250	1.51
C_1	39.999	16.043	-82.550	4.600	0.0080	1.50
C_2	1.865	30.070	32.250	4.884	0.0980	1.50
C_3	0.648	44.097	96.650	4.246	0.1520	1.50
nC_4	1.125	58.124	152.050	3.800	0.1930	1.50
nC_5	2.343	72.151	196.450	3.374	0.2510	1.50
C_6	3.689	86.178	234.250	2.969	0.2960	1.50
PC_1	24.173	102.692	312.170	2.870	0.1092	9.92
PC_2	14.513	170.586	428.490	2.168	0.1920	7.39
PC_3	8.611	287.488	570.740	1.585	0.3279	7.18
PC_4	3.035	815.804	967.610	0.953	0.6968	7.94

Table A-2—Binary interaction parameters for the CO_2/live oil mixtures after EOS calibration. "PC" stands for pseudo component.

	CO_2	C_1	C_2	C_3	C_4	C_5	C_6	PC_1	PC_2	PC_3	PC_4
CO_2	0.0000										
C_1	0.1300	0.0000									
C_2	0.1200	0.0420	0.0000								
C_3	0.1200	0.0420	0.0400	0.0000							
C_4	0.1200	0.0420	0.0400	0.0300	0.0000						
C_5	0.1200	0.0420	0.0400	0.0300	0.0116	0.0000					
C_6	0.1200	0.0420	0.0400	0.0300	0.0155	0.0058	0.0000				
PC_1	0.1200	0.0501	0.0414	0.0321	0.0343	0.0192	0.0000	0.0000			
PC_2	0.1200	0.0548	0.0420	0.0348	0.0517	0.0404	0.0000	0.0000	0.0000		
PC_3	0.1200	0.0628	0.0429	0.0434	0.0666	0.0646	0.0000	0.0000	0.0000	0.0000	
PC_4	0.0850	0.0991	0.0474	0.0737	0.0834	0.1014	0.0000	0.0000	0.0000	0.0000	0.0000

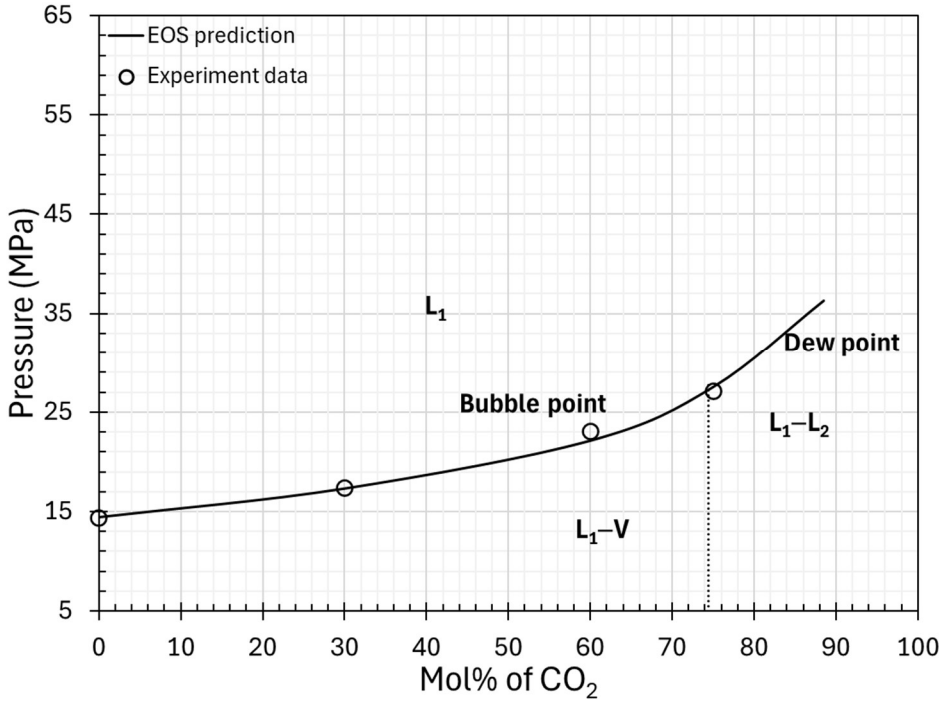

Figure A-2—Swelling test results for the pseudo-binary of CO_2 and live oil. The last mixture in the swelling test with 75 mol% CO_2 and 25 mol% oil showed a dew point; therefore, the boundary between L_1-V and L_1-L_2 was qualitatively made near the CO_2 concentration.